Some progress on CFD high lift prediction using metric-based anisotropic mesh adaptation

Frederic Alauzet, Francesco Clerici, Adrien Loseille, Cosimo Tarsia-Morisco, Julien Vanharen

Some progress on CFD high lift prediction using metric-based anisotropic mesh adaptation

Frédéric Alauzet[*], Francesco Clerici[†], Adrien Loseille [‡], Cosimo Tarsia Morisco[§], and Julien Vanharen[¶]

GAMMA Team, Inria Saclay Ile-de-France, Palaiseau, France

DMPE, ONERA, Univerité Paris Saclay, F-92322 Châtillon, France

This papers points out some weaknesses of the solution-adapted process presented in.[3] They have been solved by improving the Newton's method of the flow solver enabling convergence to machine zero at each run of the solution adaptive process. This work also presents the benefits of using metric-based anisotropic mesh adaptation for the numerical simulation of high lift configurations. For instance, we reconsider the CRM-HL geometry of the 3rd AIAA CFD High Lift Prediction Workshop and we obtain a prediction of the lift value similar to that of the x-fine mesh generated with the best practices (206 million vertices) with an adapted mesh composed only of 2.7 million vertices. This represents a reduction in the mesh size by a factor of 75.

I. Introduction

The generation of meshes for accurate and reliable numerical simulations of Reynolds-Averaged Navier-Stokes (RANS) applications is a time consuming and tedious task. Traditional processes rely on the experience and intuition of a skilled engineer to predict the flow and to manually adapt the mesh prescription to the flow. Following meshing guidelines slows down the mesh generation process and leads to a prohibitive cost in CPU time in the numerical simulation pipeline. This lack of automation is an impediment for many applications such as shape optimization. Moreover, with complex geometries and flow patterns, it is almost impossible for a user to accurately analyze the various physical features involved and prescribe an appropriate mesh. *A-priori* refinements of large zones are used instead, leading to the unnecessary consumption of large amounts of resources. This is why mesh adaptation strategies that automatically analyze the flow solutions and adapt the mesh to it can bring a significant improvement in terms of CPU times, memory consumption and accuracy through error control. This will be automatic, independent of the initial mesh and, importantly, it will remove human intervention from the numerical simulation pipeline.[8,10]

Metric-based anisotropic mesh adaptation has been very successful in predicting engineering output functional in aeronautics[3] and turbomachinery.[4] However, we still pursue the quest of getting accurate numerical prediction with the less computational resources as possible. To this end, each stage of the mesh adaptation loop is a source of improvements. For instance, the goal-oriented error estimate has been improved in a series of papers. In,[6] a first version of the goal-oriented error estimate has been proposed which was efficient for laminar flows but not RANS. A first improved version has been proposed in[18] and the current version, which is efficient for RANS, has been thoroughly detailed in.[3] In this work, we discuss improvements made on the flow solver side in the context of high-lift prediction applications.

Indeed, we applied our solution-adaptive process to the high-lift version of the NASA CRM (CRM-HL) geometry chosen for the 4th AIAA CFD High Lift Prediction Workshop (HLPW4). The considered

[*]Senior Researcher, AIAA Associate Fellow, Frederic.Alauzet@inria.fr

[†]PhD Student, Francesco.Clerici@inria.fr

[‡]Research Scientist, Adrien.Loseille@inria.fr

[§]Research Engineer, Cosimo.Tarsia-Morisco@inria.fr

[¶]Research Engineer, Julien.Vanahren@onera.fr

geometry was the one with inboard/outboard trailing-edge (TE) flap deflection 40°/37° with a nominal 30°/30° inboard/outboard leading-edge (LE) slat setting, nacelle, pylon, nacelle chine, LE brackets, TE support fairings, but no landing gear, horizontal or vertical tail. This geometry is a lot more complex than the one of the 3rd AIAA CFD High Lift Prediction Workshop (HLPW3), as shown in Figure 1. The resulting physics is richer and consequently make this case a lot more challenging. Despite the fact that we obtained very accurate results on the HLPW3 geometry,[3] we observed Lyapunov stability issues with the flow solver. We were also able to reproduce this issue on the 2-D section of the CRM-HL configuration with slat, main, and flap elements on very fine adapted meshes.

This paper discusses progress made on the flow solver to solve that issue. To this end, the Newton's method employed has been improved. The benefits of this enhancement are evaluated on the 2D CRM-HL airfoil and on the CRM-HL geometry of the 3rd AIAA CFD High Lift Prediction Workshop.

II. Anisotropic mesh adaptation algorithm with mesh-convergence analysis

A. Classical algorithm: $\mathcal{C}$-continuation method

Mesh adaptation is a non-linear problem where the couple formed by the mesh and the solution needs to be converged at the same time. The goal is to generate an optimal adapted mesh for the computed solution for a prescribed mesh size (*i.e.,* a prescribed number of vertices or mesh complexity). Therefore, an iterative process is required which is achieved by means of a mesh adaptation loop starting from an initial mesh $\mathcal{H}_0$, an initial solution W_0, an initial adjoint state W_0^* if goal-oriented mesh adaptation is considered, and a given mesh complexity $\mathcal{C}$ (the continuous counterpart of the mesh size).

At each step of the mesh adaptation loop, a metric tensor $\mathcal{M}_i$ is computed from the triple $(\mathcal{H}_i, W_i, W_i^*)$ and the given mesh complexity $\mathcal{C}$, using the selected error estimate. The metric tensor field $\mathcal{M}_i$ contains

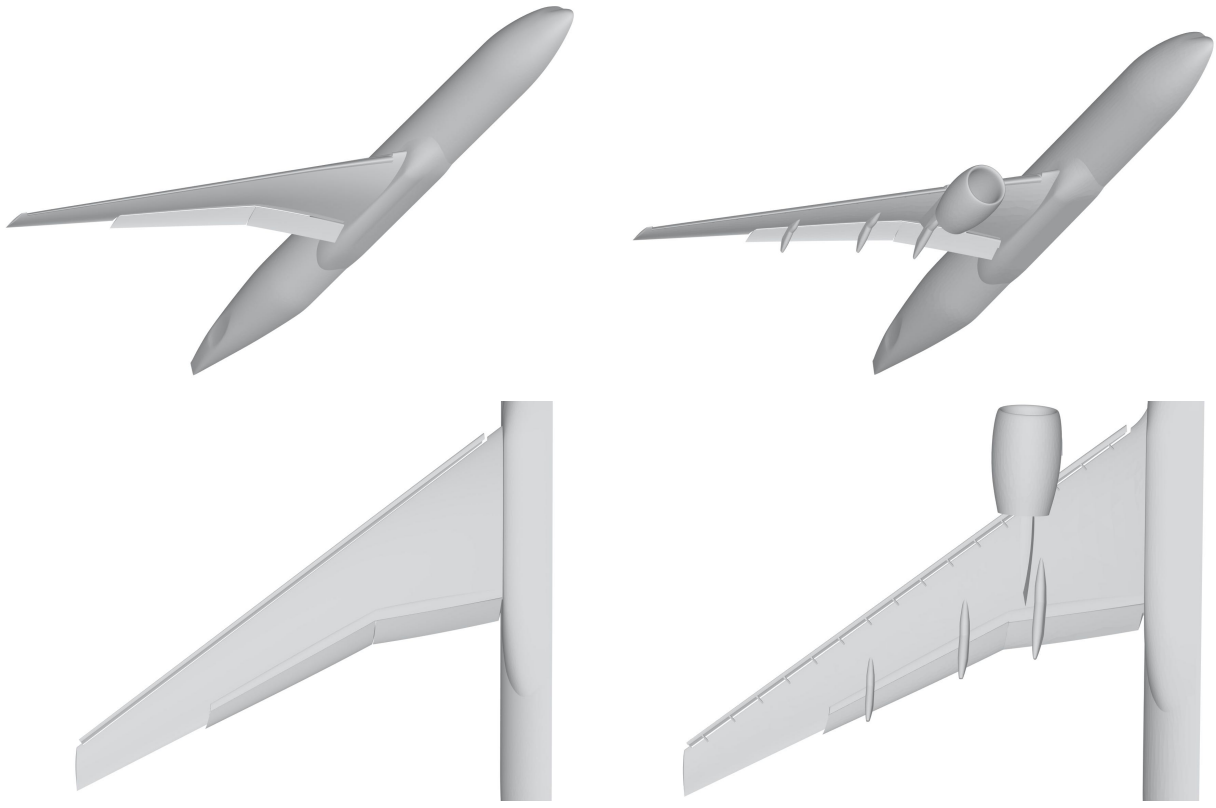

Figure 1. NASA High-Lift Common Research Model (CRM-HL) geometries. Left, geometry of the 3rd AIAA CFD High Lift Prediction Workshop (HLPW3). Right, geometry of the 4th AIAA CFD High Lift Prediction Workshop (HLPW4).

information on sizes and directions of the elements of the adapted mesh we seek. This information is then used by the remesher to generate a new adapted mesh $\mathcal{H}_{i+1}$.[16] Then W_i is interpolated on $\mathcal{H}_{i+1}$ to obtain $(W^0)_{i+1}$ which is then used as a restart solution for the next flow solution of the mesh adaptation loop.[1] In the case of goal-oriented mesh adaptation, the adjoint state W_i^* can be also interpolated on the new mesh $\mathcal{H}_{i+1}$ to obtain $(W^{*,0})_{i+1}$ which is used as a restart for the next adjoint solution. Restarts are important to not waste time in the adaptive process and reuse at maximum the previous work done. Finally, a new solution W_i and a new adjoint W_i^* fields are computed. Solution and adjoint fields are converged to machine zero at each iteration. This iterative process is depicted by the step 1 while loop in Algorithm 1.

The convergence criteria of step 1(f) is up to the expectations of the user, it specifies when the couple mesh-solution is considered as converged for the current complexity in the process. In this work, for aeronautics applications, we consider that the couple mesh-solution is converged at the given complexity if the lift coefficient, the pressure component of the drag and viscous component of the drag are not changing by a given percentage ϵ for three consecutive iterations. Usually, we choose ϵ between 0.001 (*i.e.,* 0.1%) and 0.01 (*i.e.,* 1%). It is important to check the convergence of all the components of the drag otherwise we may get early break because of compensation between the pressure and the viscous components on the total drag value.

Algorithm 1 General mesh adaptation algorithm with mesh-convergence analysis

Initial mesh $\mathcal{H}_0^0$, solution W_0^0, adjoint $W_0^{*,0}$, and complexity $\mathcal{C}^0$

`//--- Outer loop to perform the convergence study`

while $\mathcal{C}^j \leq \mathcal{C}^{jmax}$ **do**

`//--- Inner loop to converge the mesh adaptation at fixed complexity`

1. **while** i $\leq n_{adap}$ **do**
   (a) Compute optimal metric for the considered error estimate and complexity $\Longrightarrow \mathcal{M}_{i-1}^j$
   (b) Generate new adapted mesh $\Longrightarrow \mathcal{H}_i^j$
   (c) Interpolate primal and adjoint states on the new mesh $\Longrightarrow (W^0)_i^j$ and $(W^{*,0})_i^j$
   (d) Compute primal state $\Longrightarrow W_i^j$
   (e) Compute adjoint state $\Longrightarrow W_i^{*,j}$
   (f) **if** (convergence check) **then**
   $i = n_{adap} + 1$
   else
   $i = i + 1$
   fi

   done

2. $\mathcal{H}_0^{j+1} = \mathcal{H}_{n_{adap}}^j$; $W_0^{j+1} = W_{n_{adap}}^j$; $(W^*)_0^{j+1} = (W^*)_{n_{adap}}^j$; $\mathcal{C}^{j+1} = \alpha \cdot \mathcal{C}^j$ with $\alpha > 1$
   $j = j + 1$

done

In the context of a mesh convergence analysis this adaptation loop (step 1) has to be repeated for several increasing mesh complexities $\{\mathcal{C}^j\}_{j=1..jmax}$ with $jmax$ the number of considered complexities, *i.e.,* the total number of meshes for the mesh convergence analysis. An efficient strategy consists in converging the couple mesh-solution for a given complexity and reuse the final mesh, solution and adjoint state to initialize the next computations at an increased mesh complexity. Such a process enables a multiscale resolution of the flow by solving large scale features on coarse adapted meshes (at the smallest complexities) and the fine scale features of the flow on fine adapted meshes (at the largest complexities). This acts like a "multigrid effect[a]" and enables faster convergence on fine adapted meshes. This process is represented by the outer while loop in

[a]This is not a true multigrid because the coarse adapted meshes are not used in the flow solver to compute the solution.

Algorithm 1. We propose the following strategy to increase the complexity for the mesh convergence study. At each outer loop iteration, the complexity is increased by a factor α. In this work, we have set $\alpha = 2$ to multiply the mesh size by a factor 2 when increasing the complexity. Moreover, we have found that it is very advantageous to start at small complexities because a lot of work is done in converging the solution and these iterations are inexpensive in comparison to the largest complexities. The major large scale features of the flow such as shocks, shear layers and wakes are detected, advected and meshed on the coarse grids. They are then refined alongside the boundary layer as the discretization increases. And, as the turbulent boundary layer takes time to develop, it is very efficient to capture it on coarse adapted meshes.

We will call this method $\mathcal{C}$-continuation because the parameters of the simulation stay the same, only the mesh complexity is varying.

III. Mesh adaptation components

A. WOLF flow solver

WOLF is a vertex-centered (flow variables are stored at vertices of the mesh) mixed finite-volume - finite-element Navier-Stokes solver on unstructured meshes composed of triangles in 2D and tetrahedra in 3D.

The convective terms are solved by the finite-volume method on the dual mesh composed of median cells. It uses the HLLC approximate Riemann solver to compute the flux at the cell interface. Second order space accuracy is achieved through a piecewise linear interpolation based on the Monotonic Upwind Scheme for Conservation Law (MUSCL) procedure which uses a particular edge-based formulation with upwind elements. A specific low dissipation scheme is adopted using combination of centered (edge gradient) and upwind gradients (element gradient). A dedicated slope limiter is employed to damp or eliminate spurious oscillations that may occur in the vicinity of discontinuities. This new limiter is fully detailed in.[3] The viscous terms are solved by the P^1 Galerkin finite element method (FEM) which provides second order accuracy.

The implicit temporal discretization considers the backward Euler time-integration scheme. At each time step, the linear system of equations is approximately solved using a Symmetric Gauss-Seidel (SGS) implicit solver and local time stepping to accelerate the convergence toward the steady state. A Newton method based on the SGS relaxation is very attractive because it uses an edge-based data structure which can be efficiently parallelized.

As for the turbulence model, the negative Spalart-Allmaras (SA-neg) is loosely-coupled to the mean-flow equations, where the mean-flow and turbulence model equations are relaxed in an alternating sequence. The flow solver WOLF is thoroughly detailed in[3] with all the associated bibliography.

Since,[3] the main improvements of the flow solver for high-lift prediction applications have been made on the implicit time integration algorithm.

In order to design a true Newton's method, we have followed some of the lines of.[5,7,20] In such process, the CFL evolves depending on the behavior of the Newton's method, and an under-relaxation can applied to the increment obtained after the implicit solve. We observe that zeroing some of the increments was an impediment to the converge to machine zero. Moreover, a key improvement is to check whether the current non-linear residual has been decreased by the implicit solve:

$$\left\| \mathbf{R}(W^{n+1}) + \frac{|C|}{\Delta t} \left(W^{n+1} - W^n \right) \right\| \leq \|\mathbf{R}(W^n)\| \ ,$$

instead of checking the reduction of the residual: $\left\|\mathbf{R}(W^{n+1})\right\| \leq \|\mathbf{R}(W^n)\|$. This change enables the CFL to growth faster resulting in faster convergence to machine zero or, convergence to machine zero when the previous version stalls. This is illustrated on the 2D zero pressure gradient flat plate test case proposed on the NASA Turbulence Resource website. Figure 2 (left) shows that the new Newton's method reduces by a factor 2 the number of iterations required to converge to machine zero. The benefits in the CFL evolution is pointed out in Figure 2 (right).

As stated in the introduction, we observed Lyapunov stability issues with the previous implicit scheme on the HLPW4 geometry. In other words, force and moment values were oscillating periodically around a fixed value without converging toward that value, assuming that the RANS modeling provides a steady solution

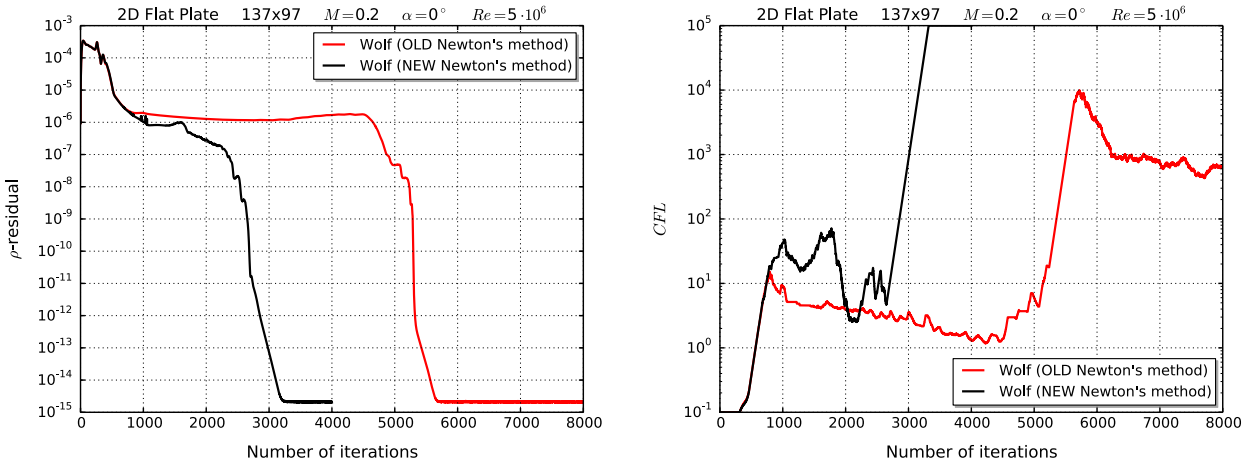

Figure 2. 2D Zero Pressure Gradient Flat Plate. Left, ρ-residual obtained with the previous and the new Newton's method. The number of iterations to converge to machine zero has been reduce by a factor 2. Right, evolution of the CFL during the simulation. Checking for non-linear residual decrease enables the CFL to grow rapidly while checking for residual decrease prevents the CFL from growing to high values.

in that case and we are not considering an unsteady case. We were able to reproduce this issue on the 2-D CRM-HL airfoil with slat, main, and flap elements on extremely fine adapted meshes where the numerical dissipation is very low. This stability issue in shown in Figure 3 (left).

This issue comes from the Symmetric Gauss-Seidel (SGS) implicit solver which is not strong enough to achieve machine-zero convergence. We tried a GMRES implicit solver preconditioned with SGS relaxation but it was not helping. We have been able to solve that issue by developing a non-linear SGS solver consisting in coupling the SGS with fixed point iterations. Figure 3 (right) shows that there is no oscillation in the lift history, even on extremely fine adapted meshes. Moreover, the non-linear SGS can also bring improvement in efficiency as pointed out in Figure 4. It reduces the number of iterations required to converge to machine zero, mainly because more SGS sweeps are performed at each flow solver iteration. This can also lead to a reduction of the CPU time.

These improvements are another step forward in designing of a finite volume strong solver.

B. Wolf adjoint solver

As regards the adjoint state computation, needed for goal-oriented error estimates, the matrix of the linear system is simply the implicit matrix (without the mass matrix) transposed and the right hand-side of the system is the chosen functional (for instance, drag, lift, ...) exactly differentiated. In particular, for viscous flows, μ and the stress tensor τ are exactly differentiated. In order to solve the adjoint system, we use a restarted GMRES preconditioned with SGS relaxations. Note that, it is important to converge the adjoint problem to machine zero to obtain an accurate adjoint state for mesh adaptation.

C. Feflo.a local adaptive remesher

Feflo.a is a generic purpose adaptive mesh generator dealing with 2D, 3D and surface mesh generation. It belongs to the class of metric-based mesh generator which aims at generating a unit mesh with respect to a prescribed metric field $\mathcal{M}$. A mesh is said to be unit when composed of almost unit-length edges and unit-volume element.

The adaptive remesher is based a combination of generalized standard operators (insertion, collapse, swap of edges and faces). The generalized operators are based on recasting the standard operators in a cavity framework.[14,16] Additional modifications on the cavity allow to either favor a modification, that would have been rejected with the standard operator, or to improve the final quality by combining automatically many standard operators at once. In addition, the CPU time is also improved and becomes independent of the current modification. The unit speed is around $20,000$ points inserted or removed per second on Intel

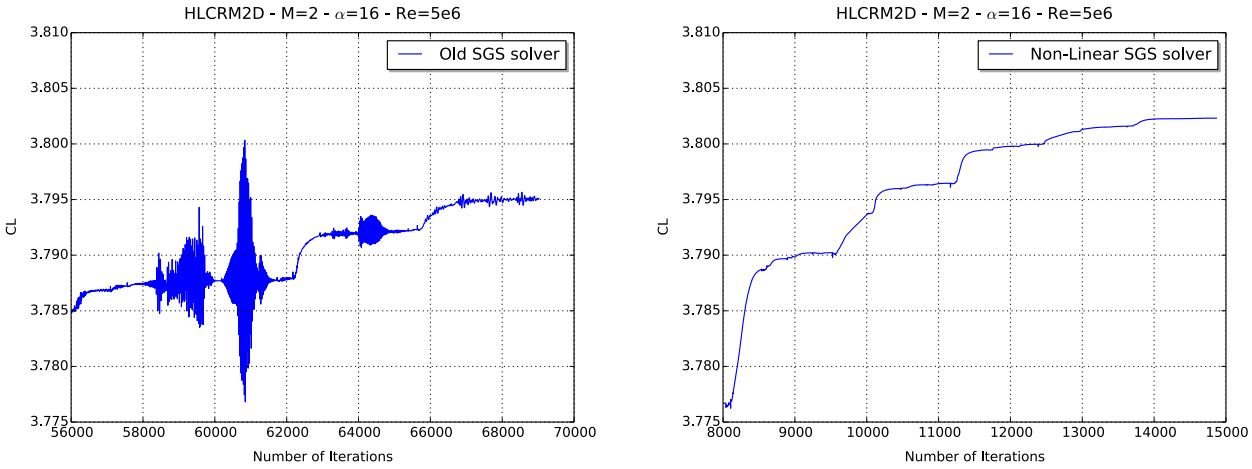

Figure 3. CRM-HL airfoil. History of the lift during the solution adaptive process. Left, oscillations in the lift prediction obtained with the SGS implicit solver. Right, no oscillation is observed in the lift prediction with the non-linear SGS implicit solver.

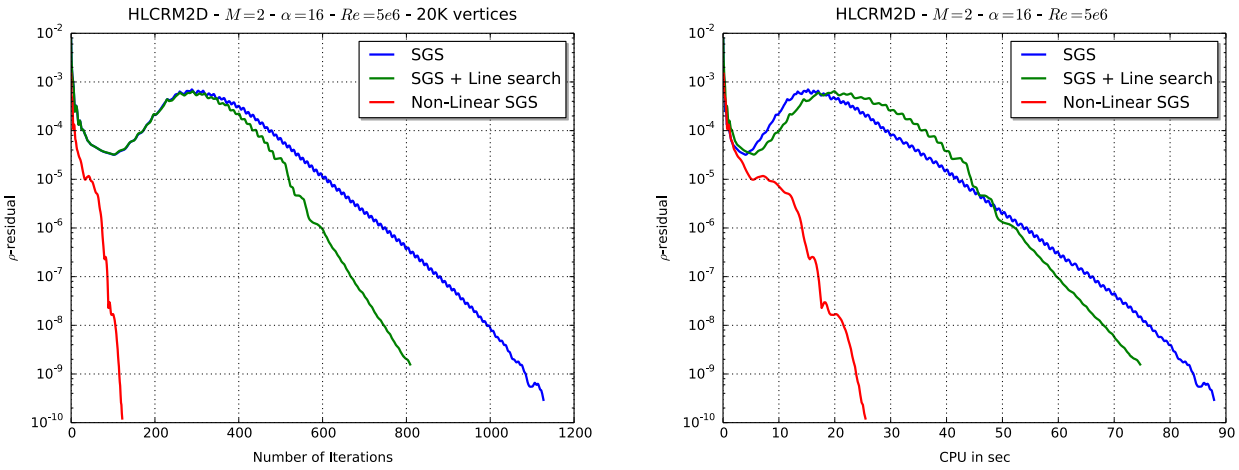

Figure 4. CRM-HL airfoil. ρ-residual history on an adapted mesh composed 20K vertices with respect to the number of iterations (left) and the CPU time in second (right). In blue, behavior of the classical SGS implicit solver. In green, behavior of the classical SGS implicit solver coupled with a line search. In red, behavior of the non-linear SGS implicit solver. We note that the non-linear SGS solver reduces the number of iterations to converge to machine zero almost by a factor 10 and the CPU time by a factor 3.5.

i7 architecture at 2.7 GHz. For robustness purpose, both the surface and the volume mesh are adapted simultaneously, and each local modification is checked to verify that a valid mesh is obtained. For the volume, the validity consists in checking that each newly created element has a strictly positive volume. For the surface, the validity is checked by ensuring that the deviation of the geometric approximation with respect to a reference surface mesh remains within a given tolerance.

The generation of a unit mesh is decomposed into two steps:

1. Generate a unit-mesh : the mesh modification operators are used in the goal to optimize the length of the edges in $\mathcal{M}$.

2. Optimization: the mesh modification operators are used to improve the quality $Q_{\mathcal{M}}$.

During surface remeshing, either a P3 background surface is used or a direct CAD queries is used. The CAD kernel is based on EGADS and OpenCascade.[11]

D. RANS goal-oriented error estimate

A goal-oriented error estimate based on an *a priori* error analysis has initially been proposed for the inviscid Euler equations in.[15] The main idea was to translate the error on the considered output functional into a weighted interpolation error estimate. Weights are given by derivatives of the adjoint state and interpolation errors are on the Euler fluxes. As we are left with weighted interpolation errors, we can use the continuous mesh framework[12,13] to obtain an analytical expression of the optimal metric field. An extension of this goal-oriented error estimate has been proposed for the laminar Navier-Stokes equations in.[6] The main advantage of these error estimates in comparison to other goal-oriented error estimates is that the anisotropy of the mesh appears naturally.

From the analysis of the behavior several error estimates for the Reynolds Averaged Navier-Stokes equations,[18] we came up with the following new goal-oriented error estimate for RANS using integration by part and linearization:[3]

$$|J(W) - J(W_h)| \;\leq\; \int_\Omega \left| -\frac{\partial J}{\partial W} + \sum_i \left(\frac{\partial \mathcal{F}_i^E}{\partial W}\right)^T \nabla_{x_i} W^* + \sum_{i,j} \left(\frac{\partial \mathcal{F}_i^V}{\partial \nabla_{x_j} W}\right)^T W^*_{x_i,x_j} \right| \left|W - \Pi_h W\right| \mathrm{d}\Omega \quad (1)$$

where J is the considered output functional, W is the conservative variables vector, W^* the associated adjoint state, $\mathcal{F}^E$ the convective fluxes, $\mathcal{F}^V$ the viscous fluxes, $\nabla_{x_i} W^*$ and $W^*_{x_i,x_j}$ the gradient and the hessian of the adjoint state. The error estimate is a weighted sum of L^1 interpolation error on the conservative variables where the weights depend on the gradient and the hessian of the adjoint state and on the convective and viscous fluxes. Therefore, we can directly apply the continuous mesh framework to obtain an analytical expression of the optimal metric field.[3]

IV. High Lift Common Research Airfoil

We consider a two-dimensional (2-D) multi-element airfoil configuration which is a 2-D section of the wing of the CRM-HL geometry with slat, main, and flap elements. We will call it CRM-HL airfoil. It corresponds to case 3 of the the 4$^{\text{th}}$ AIAA CFD High Lift Prediction Workshop. The flow conditions are:

Mach number	Angle-of-attack	Reynolds number based on L_{ref}	Temperature (K)
0.2	16	5.e6	272.1

The case is considered in SI units with a reference length of 1 m.

Several solution-adaptive strategies were compared in,[19] most of them considering a finite element flow solver. The only finite volume flow solver was Wolf. All methodologies were converging toward samilar force and moment values. However, a slight under-prediction of the lift (≈ 3.795 vs ≈ 3.802, *i.e.* 0.7 lift counts) and over-prediction of the drag (≈ 0.0609 vs ≈ 0.0606, *i.e.* 3 drag counts) was observed for the finite volume flow solver. We demonstrate in this section that a strong finite volume solver would not produce that small discrepancy.

For the mesh adaptation, the RANS goal-oriented error estimate is considered with the lift as output functional. For each complexity, we perform a maximum of $n_{adap} = 15$ mesh adaptation iterations and we choose $\epsilon = 0.003$ as threshold to exit the mesh adaptation loop at each complexity. We consider nine complexities for the convergence study:

$$\{4\,000,\ 8\,000,\ 16\,000,\ 32\,000,\ 64\,000,\ 128\,000,\ 256\,000,\ 512\,000,\ 1\,024\,000\}\ .$$

We start the convergence study with an initial coarse mesh composed of 2 651 vertices and 4 616 triangles, see Figure 5. This is a simple inviscid mesh without any boundary layer or any specific refinement for viscous flows, thus very easy and quick to generate.

We analyse the obtained result on a medium size adapted mesh composed of 74 442 vertices and 144 321 triangles (obtained for a complexity of 64 000) and a fine size adapted mesh composed of 587 826 vertices and 1 163 564 triangles (obtained for a complexity of 512 000). The medium and fine adapted meshes are shown in Figures 7 and 8. The velocity field on the fine adapted mesh is depicted in Figure 6. We observe the adaptation of the mesh is resolving important flow features, such as the attached and off-body shear layers, suction peaks on the upper surfaces, gaps between the slat/wing and wing/flap, and the stagnation

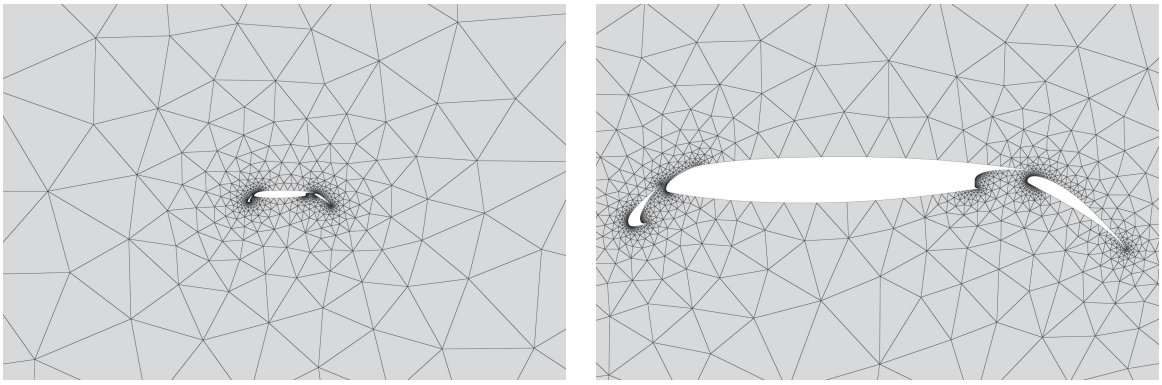

Figure 5. CRM-HL airfoil. Initial mesh composed of 2 651 vertices and 4 616 triangles..

Medium adapted mesh		
Anisotropic ratio	CRM-HL Airfoil	
$1 < \text{ratio} \leq 2$	47 001	32.57 %
$2 < \text{ratio} \leq 3$	6 768	4.69 %
$3 < \text{ratio} \leq 4$	5 239	3.63 %
$4 < \text{ratio} \leq 5$	4 176	2.89 %
$5 < \text{ratio} \leq 10$	14 155	9.81 %
$10 < \text{ratio} \leq 50$	40 438	28.02 %
$50 < \text{ratio} \leq 100$	12 676	8.78 %
$10^2 < \text{ratio} \leq 10^3$	13 859	9.60 %
$10^3 < \text{ratio} \leq 10^4$	9	0.01 %
Mean ratio	34.5	

Fine adapted mesh		
Anisotropic ratio	CRM-HL Airfoil	
$1 < \text{ratio} \leq 2$	373 484	32.10 %
$2 < \text{ratio} \leq 3$	44 709	3.84 %
$3 < \text{ratio} \leq 4$	32 541	2.80 %
$4 < \text{ratio} \leq 5$	27 973	2.40 %
$5 < \text{ratio} \leq 10$	104 440	8.98 %
$10 < \text{ratio} \leq 50$	317 726	27.31 %
$50 < \text{ratio} \leq 100$	117 192	10.07 %
$10^2 < \text{ratio} \leq 10^3$	145 290	12.49 %
$10^3 < \text{ratio} \leq 10^4$	209	0.02 %
Mean ratio	42.7	

Table 1. CRM-HL airfoil. Anisotropic ratio histograms for the medium adapted mesh composed of 74 442 vertices and 144 321 triangles (left) and the fine adapted mesh composed of 587 826 vertices and 1 163 564 triangles (right). For each interval, the number of triangles is given with the corresponding percentage.

Method	CL	CD	CDv	CM
GGNS-EPIC-L4	3.80170	0.060654	0.009391	-0.38290
GGNS-EPIC-Lift	3.80195	0.060673	0.009375	-0.38296
SANS-EPIC-MOES	3.80284	0.060718	0.009376	-0.38314
SFE-REFINE-MS	3.80038	0.060841	0.009370	-0.38280
Wolf-Fefloa-L4 SGS 2020	3.79323	0.060975	0.009366	-0.38142
Wolf-Fefloa-Lift SGS 2020	3.79601	0.060825	0.009343	-0.38195
Wolf-Fefloa-L4 NL-SGS 2021	3.80160	0.060601	0.009395	-0.38285
Wolf-Fefloa-Lift NL-SGS 2021	3.80232	0.060565	0.009385	-0.38298

Table 2. CRM-HL airfoil. Computed force and moment values on the finest adapted mesh for several solution adaptive process. GGNS, SANS, SFE and Wolf 2020 values come from.[19]

regions on the slat wing and flap. It also resolves the wakes where they interact with downstream geometry, but forgo refinement far downstream of the airfoil contrary to feature-based mesh adaptation. We note that the isolines have a L-shape at the upper edge of the wake showing a discontinuity of the gradient in that region. The active role played by the adjoint and the goal-oriented error estimate induces also an adaptation of the stagnation streamlines for each of the airfoil elements. However, in our case, this adaptation is less

important than the refinements obtained with dual error estimates.[9]

Table 1 provides anisotropic ratio mesh characteristics for both adapted meshes. Similarly to inviscid flows, we note that anisotropy increases with the mesh complexity. This is pointed out by the mean anisotropic ratio that increases from 34.5 to 42.7 and also the percentage of element with an anisotropic ratio between 10 and 1000 which increases from 46.4% to 49.9%.

Now, we compare the results obtained with WOLF in[19] and the new results with the improved Newton's method. First, Figure 9 emphasizes that convergence to machine zero is obtained at each run thanks to the improved Newton's method. Second, it also solves the Lyapunov stability issue. Indeed, results obtained with the previous Newton's method have some small oscillations of the force and moment values during the mesh convergence, as can be observed in Figures 10, 11, 12, and 13. On the contrary, these oscillations disappear with the new Newton's method, see Figure 3 (right), and a smooth convergence of the force and moment values is obtained, see Figures 10, 11, 12, and 13. This is emphasized in Table 2 where the slight discrepancy in the aerodynamic coefficients prediction has disappeared between the Finite Volume flow solver and the Finite Element solvers. For instance, the delta in lift value at convergence is now less than 0.2 lift count with respect to the finite element flow solvers.

In order to complete the analysis on this example, we want to point out an interesting feature of the solution-adaptive process. The y^+ prescribed by the mesh adaptation process is consistent whatever the mesh size. Indeed, in Figure 14, we plot the normal size prescription at wall the by mesh adaptation process for the medium (left) and the fine (right) adapted meshes. We note that a smaller normal mesh size is required at higher complexity which was expected. But more surprisingly, the obtained y^+ at wall is the same for both meshes as shown in Figure 15. This is logical because y^+ depends both on the mesh size but also on the skin friction, which is an output of the calculation. In conclusion, in a mesh adaptation process, the y^+ prescription is constant while the spacing normal to the wall varies which is very different from best practice process where from the simulation given Reynolds number a global normal sizing is deduced by fixing a targeted y^+.

It is thus interesting to visualize how is the adapted mesh in that region. Figure 16 (left) shows a close-up view of the adapted mesh on the upper part of the main wing where we clearly see refinements on the slat off-body shear layer which is transported above the main wing, in the boundary layer and at the upper edge of the boundary layer. When we zoom in the boundary layer, Figure 16 (right), we note that the evolution of the sizing in the normal direction is very different from best practice process. Near the wall the normal sizing is somehow larger because we are in the linear sublayer, then we have a lot of refinement in the buffer layer, and then the normal size is growing in the log-law region.

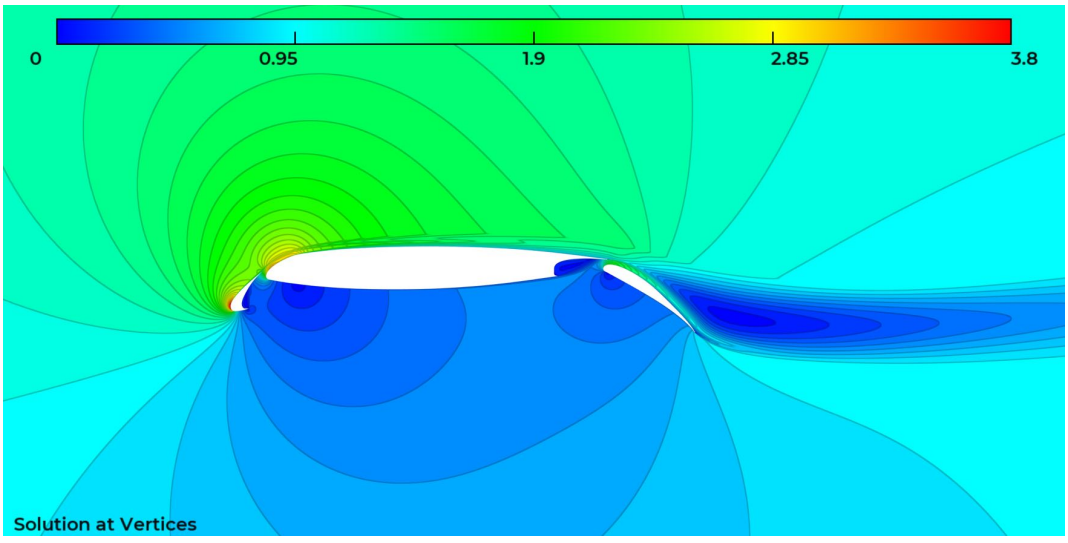

Figure 6. CRM-HL airfoil. Velocity solution obtained on the fine adapted mesh composed of 587 826 **vertices and** 1 163 564 **triangles.**

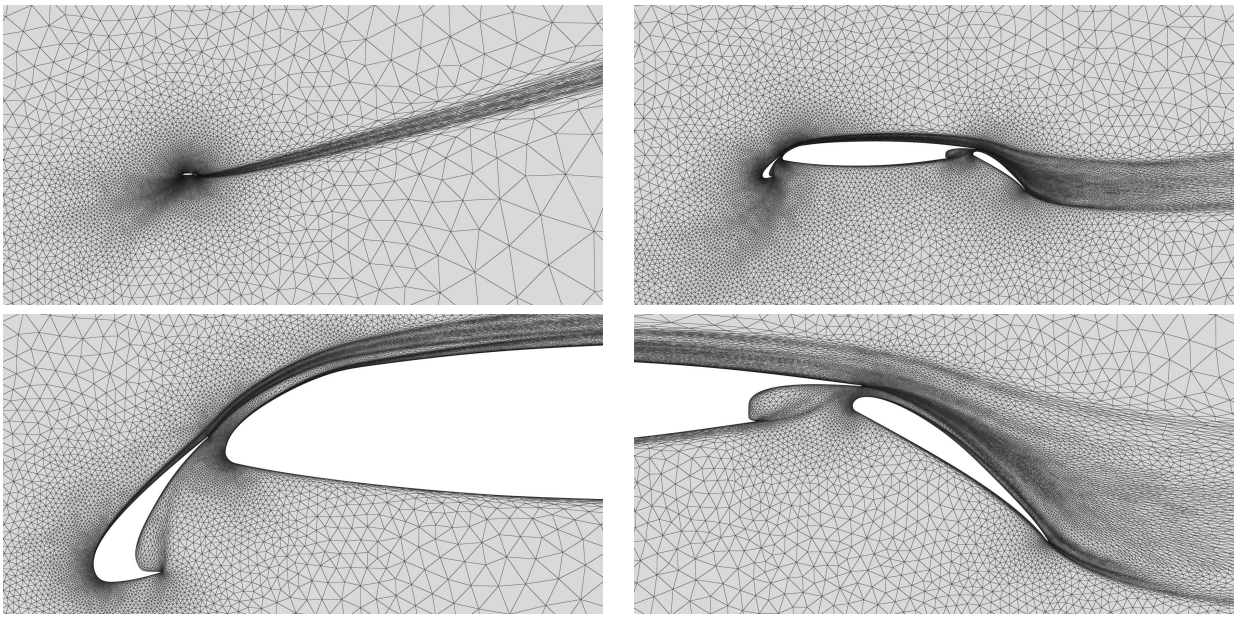

Figure 7. CRM-HL airfoil. Medium adapted mesh composed of 74 442 vertices and 144 321 triangles.

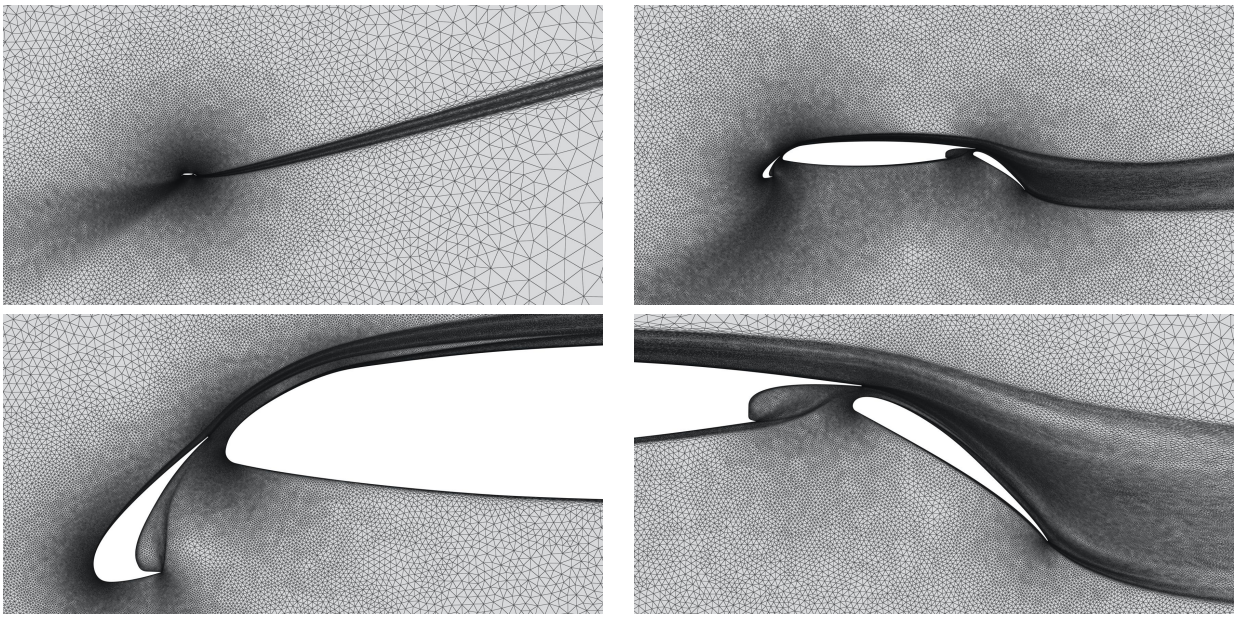

Figure 8. CRM-HL airfoil. Fine adapted mesh composed of 587 826 vertices and 1 163 564 triangles.

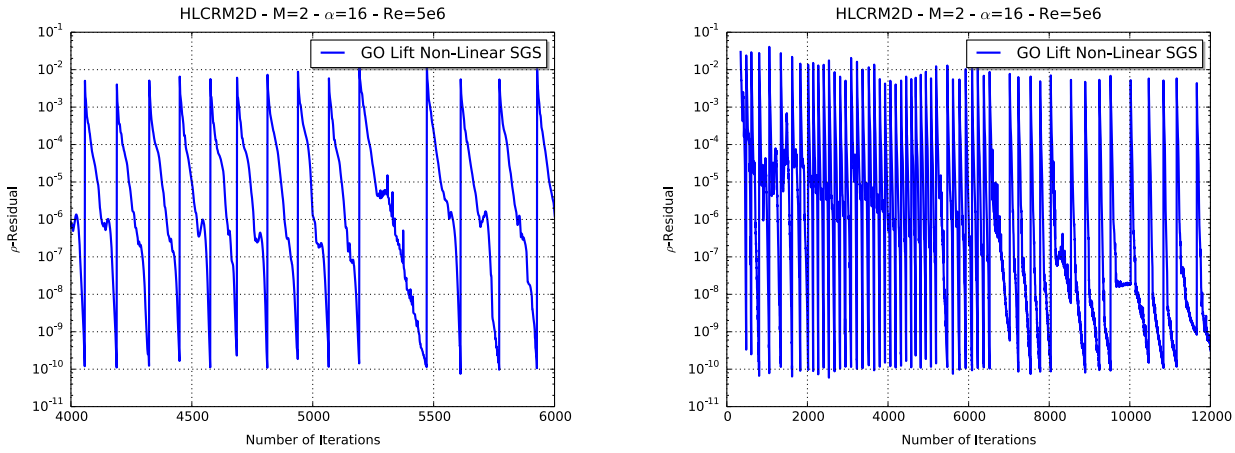

Figure 9. CRM-HL airfoil. History of the ρ-residual throughout the whole solution adaptive process. Each increases of the residual corresponds to a new run on a new adapted mesh.

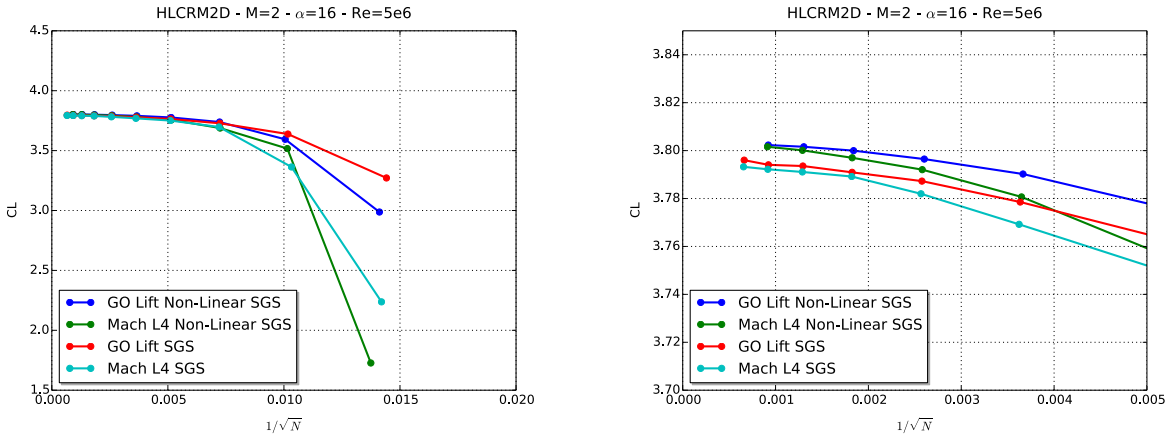

Figure 10. CRM-HL airfoil. Convergence of the total lift for the solution-adaptive process.

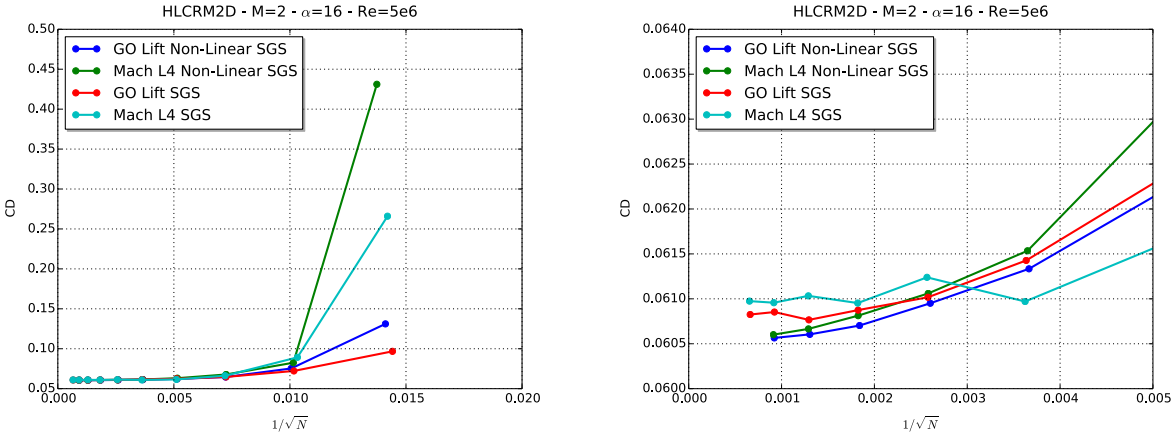

Figure 11. CRM-HL airfoil. Convergence of the total drag for the solution-adaptive process.

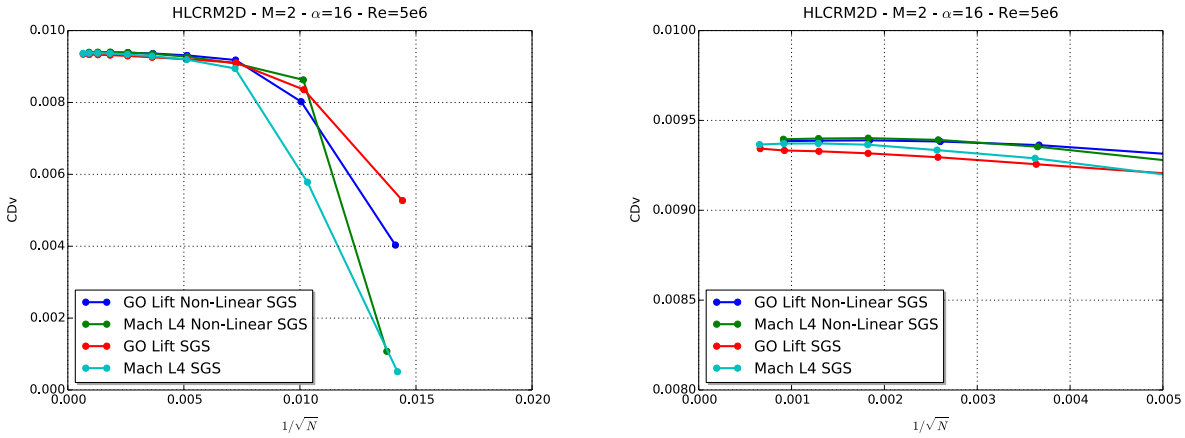

Figure 12. CRM-HL airfoil. Convergence of the viscous drag for the solution-adaptive process.

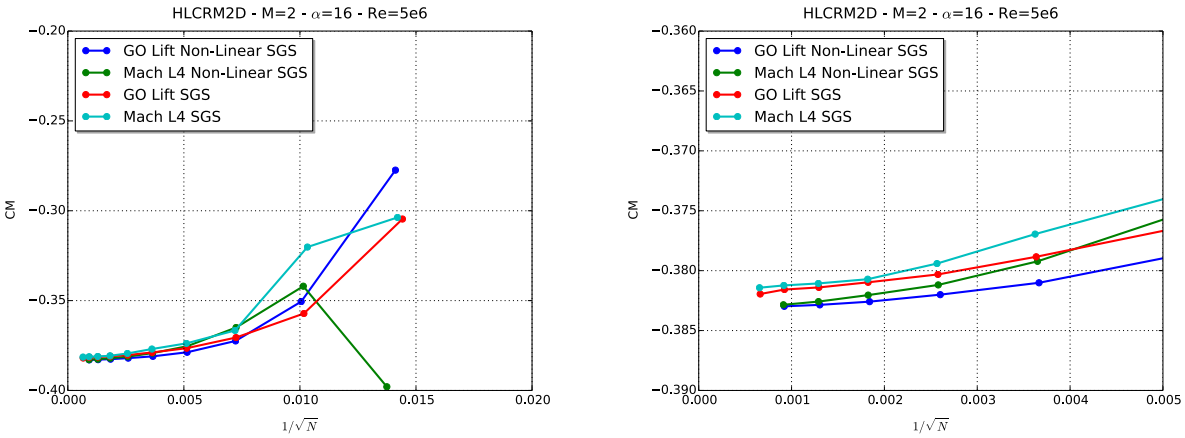

Figure 13. CRM-HL airfoil. Convergence of the moment for the solution-adaptive process.

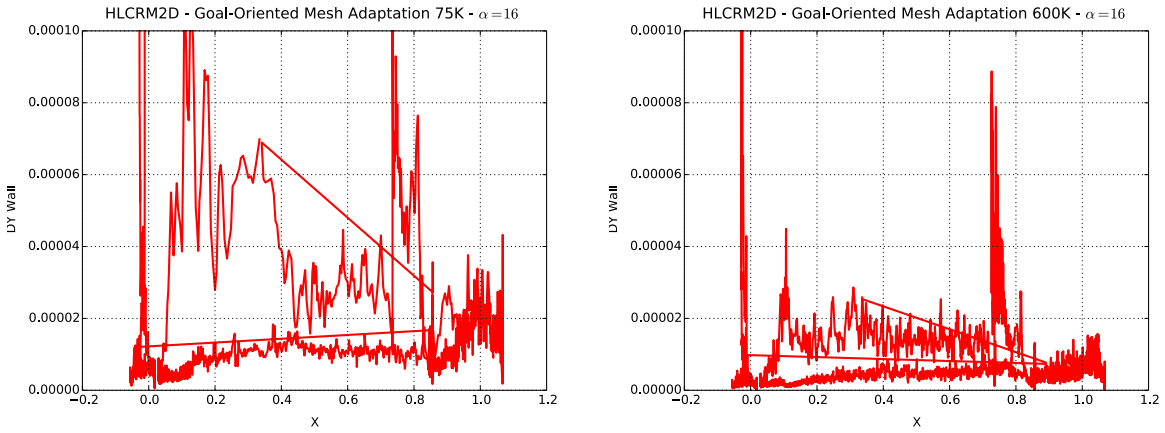

Figure 14. CRM-HL airfoil. Normal size prescription at wall by the mesh adaptation process.

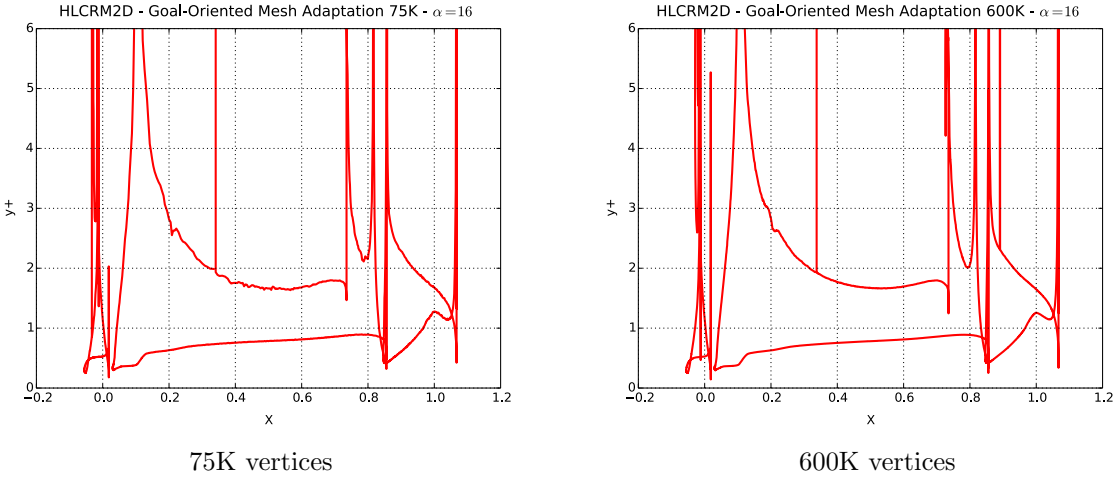

Figure 15. CRM-HL airfoil. y^+ prescription at wall by the mesh adaptation process.

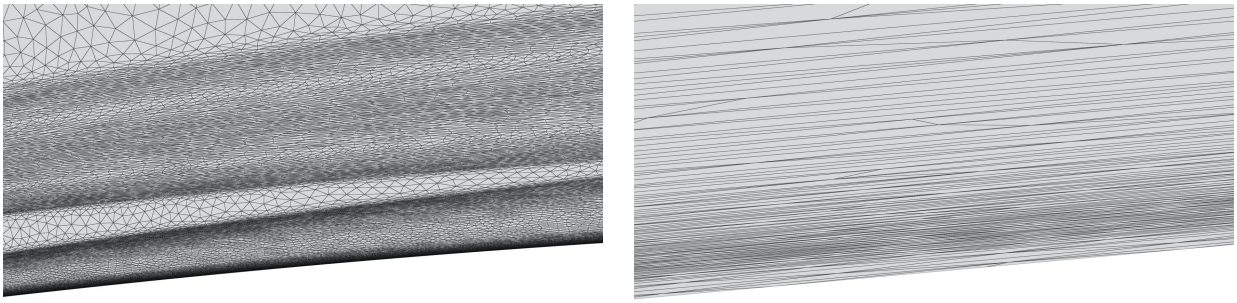

Figure 16. CRM-HL airfoil. Fine adapted mesh composed of 587 826 vertices and 1 163 564 triangles. View of the mesh on the upper part main wing and a zoom in the boundary layer region.

V. High Lift Common Research Model of the 3rd AIAA CFD High Lift Prediction Workshop

We consider the high-lift version of the NASA CRM (CRM-HL) geometry used for the 3rd AIAA CFD High Lift Prediction Workshop[21] (HLPW3), see Figure 1 (left). We select the geometry with the full chord flap gap which corresponds to the case 1b of the workshop with the following flow conditions:

Mach number	Angle-of-Attack	Reynolds number	Temperature (K)
0.2	16	3.26e6	288.15

The case is considered in SI units. The geometry has been transformed in meters, so in that case the reference length is 7.00532 m and the reference surface is 191.84477 m^2. This simulation was already analyzed in[2] and,[3] thus the interest in showing the obtained enhancement thanks to the flow solver improvements.

For the mesh adaptation, the RANS goal-oriented error estimate is considered with the lift as output functional. For each complexity, we perform a maximum of $n_{adap} = 15$ mesh adaptation iterations and we choose $\epsilon = 0.003$ as threshold to exit the mesh adaptation loop at each complexity. We consider nine complexities for the convergence study:

$$\{320\,000,\ 640\,000,\ 1\,280\,000,\ 2\,560\,000,\ 5\,120\,000,\ 10\,240\,000\}\ .$$

For the given complexities, we end-up with final adapted meshes of size between $0.65M$ and $20M$ vertices. The explanation of the factor two between the mesh complexity and the number of vertices is given in.[17]

We start the convergence study with an initial very coarse mesh only composed of 51 314 vertices, 265 482 tetrahedra and 26 692 triangles on the surface, see Figure 17. This is a simple inviscid mesh without any boundary layer or any specific refinement for viscous flows, thus very easy and quick to generate. We choose to start from this coarse and clearly unresolved mesh to illustrate the non-dependency of the solution-adaptive process to the initial data.

We compare the results obtained with the solution-adaptive process to all the results obtained during the workshop on the coarse (8M vertices), the medium (26M vertices), the fine (70M vertices) and the x-fine (206M vertices) meshes. In Figures 21 and 22 we compare the lift and drag prediction results obtained with the solution-adaptive process (blue stars) with respect to all the HLPW3 results (red squares).

For the lift prediction, see Figure 21, we observe that a result similar to the fine grid is obtained with a 1.3M vertices adapted mesh, and the 2.73M and 5.40M vertices adapted meshes provides results similar to the x-fine mesh that have been run by only five participants. We are predicting a lift value of 2.382 which is above the one of the workshop on the x-fine mesh, *i.e.* 2.365. Seeing that workshop lift values tend to increase with the mesh size, it may state that even with the x-fine mesh the solution is not yet mesh-converged.

The drag prediction requires larger adapted meshes, 5.41M to 10.5M vertices adapted meshes are needed to get a drag value corresponding to the one obtained on the x-fine grid.

In conclusion, we achieve the same accuracy as meshes done with the best practice meshing guidelines but with 75 times less vertices for the lift prediction and 20 to 40 times less vertices for the drag prediction.

The convergence of the lift and the drag value throughout the whole mesh-convergence analysis is shown in Figure 18. It shows the evolution of the lift and the drag values for each computation in red (*i.e.,* each adaptation at each complexity) and the final retained values obtained for each complexity in blue. As in 2D, we note that a lot is done on coarse adapted meshes (which is cheap) while a minimum number of iterations is done on the finer adapted meshes. Converging on coarse meshes is advantageous and enable early capturing of the solution. Moreover, these plots point out that we are able to achieve mesh-convergence for this 3D case.

In order to emphasize that we achieve mesh-convergence, we plot our lift convergence results with respect to all the workshop results in Figure 19. Workshop entries are plotted with green lines, feature-based mesh adaptation results with red lines, and goal-oriented mesh adaptation results with blue lines. Label Wolf19 corresponds to results in,[2] label Wolf20 corresponds to results in,[3] and label Wolf21 corresponds to the current results. We clearly see the improvement in the prediction thanks to the improvements in the finite volume flow solver, and the higher lift prediction obtained by the solution adaptive process.

Finally, in Figure 20, we show views of the adapted mesh composed of 10.5M vertices and its associated local Mach number field in the slat and the flap regions. It points out the highly resolved adapted mesh obtained by the solution-adaptive process. Similarly to the 2D case, the adaptation of the mesh is resolving important flow features, such as the attached and off-body shear layers, suction peaks on the upper surfaces, gaps between the slat/wing and wing/flap, and the stagnation regions on the slat wing and flap. It also resolves the wakes where they interact with downstream geometry. Again, we clearly see that the isolines are L-shape at the upper edge of the wake showing a discontinuity of the gradient in that region.

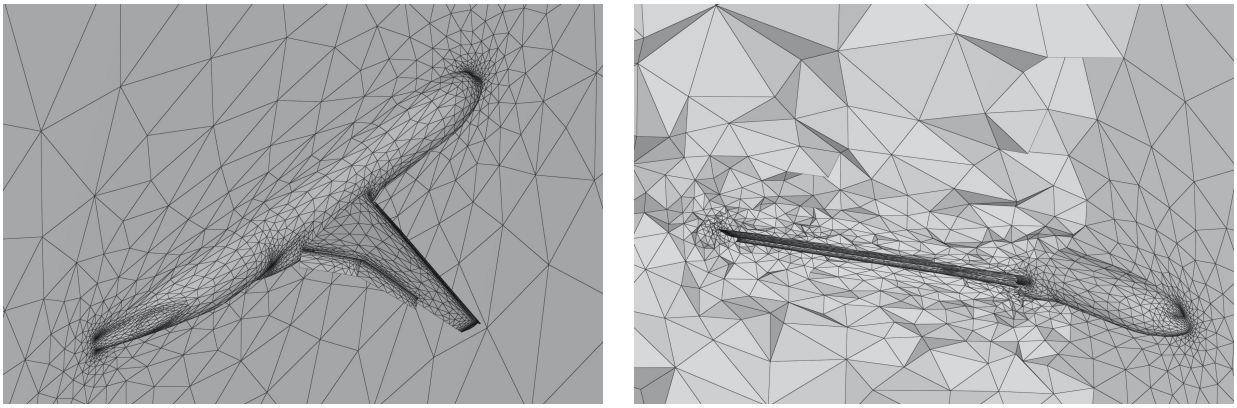

Figure 17. HLPW3 CRM-HL 16° **case. Initial coarse and clearly unresolved mesh only composed of** 51 314 **vertices,** 265 482 **tetrahedra and** 26 692 **triangles on the surface.**

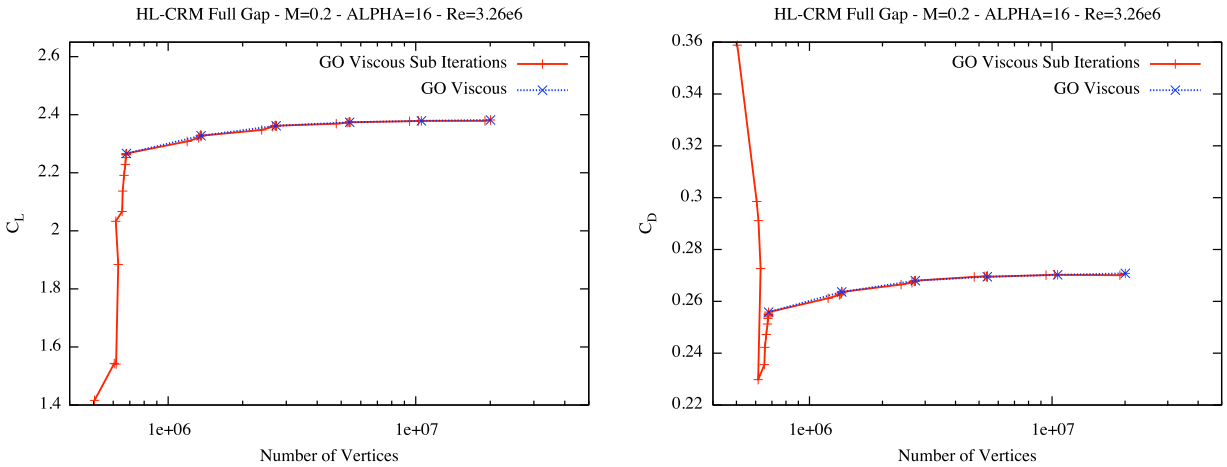

Figure 18. HLPW3 CRM-HL 16° **case. Convergence history of the total lift value C_L (left) and total drag value (right) for the viscous goal-oriented error estimate throughout the whole mesh-convergence analysis. In red, the convergence of the total lift at each complexity and, in blue, the global convergence of the total lift by retaining the final lift value for each complexity.**

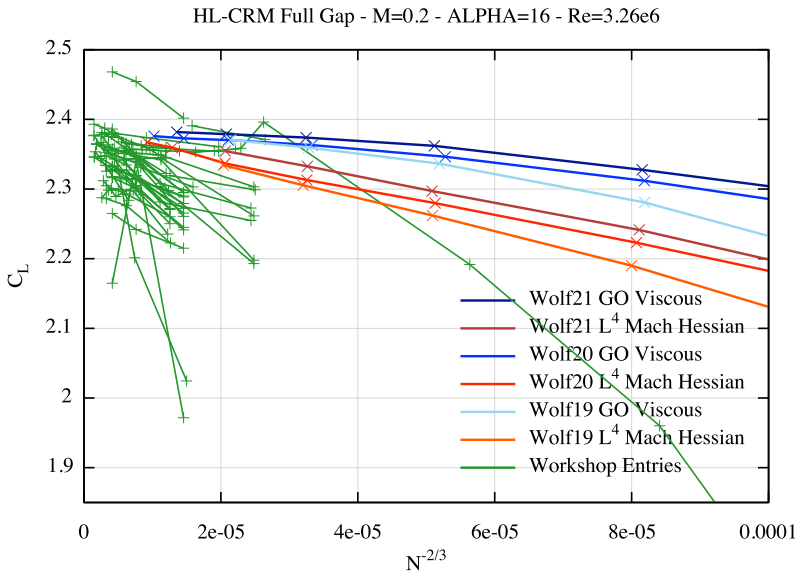

Figure 19. HLPW3 CRM-HL 16° **case. Convergence of the total lift for the solution-adaptive process with the feature-based error estimate (red lines) and the viscous goal-oriented error estimate (blue lines) with respect to all workshop entries (green lines). Wolf19 corresponds to results in,[2] Wolf20 corresponds to results in,[3] and Wolf21 corresponds to the current results.**

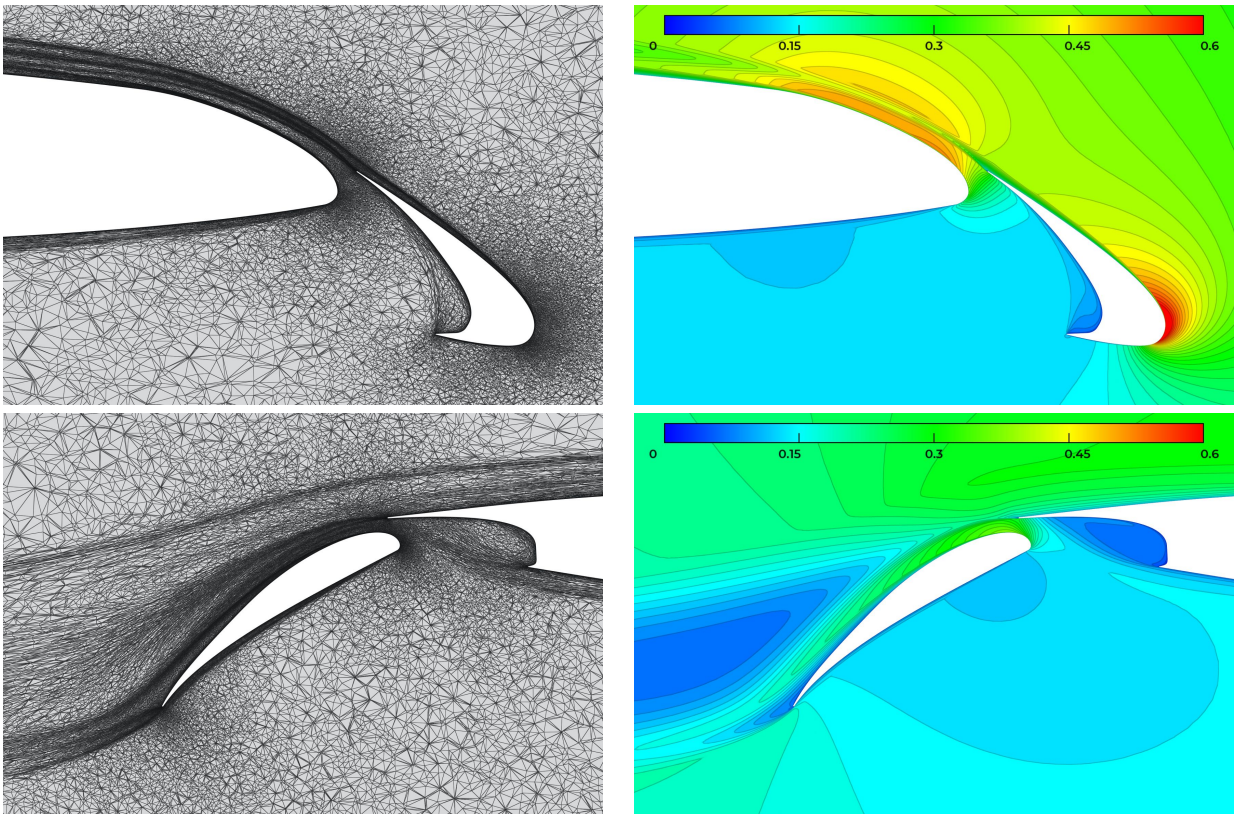

Figure 20. HLPW3 CRM-HL 16° **case. Adapted mesh composed of 10.5M vertices and associated solution field (local Mach number) for the cut plane** $y = 15.5$ **in the slat region (top) and the flap region (bottom).**

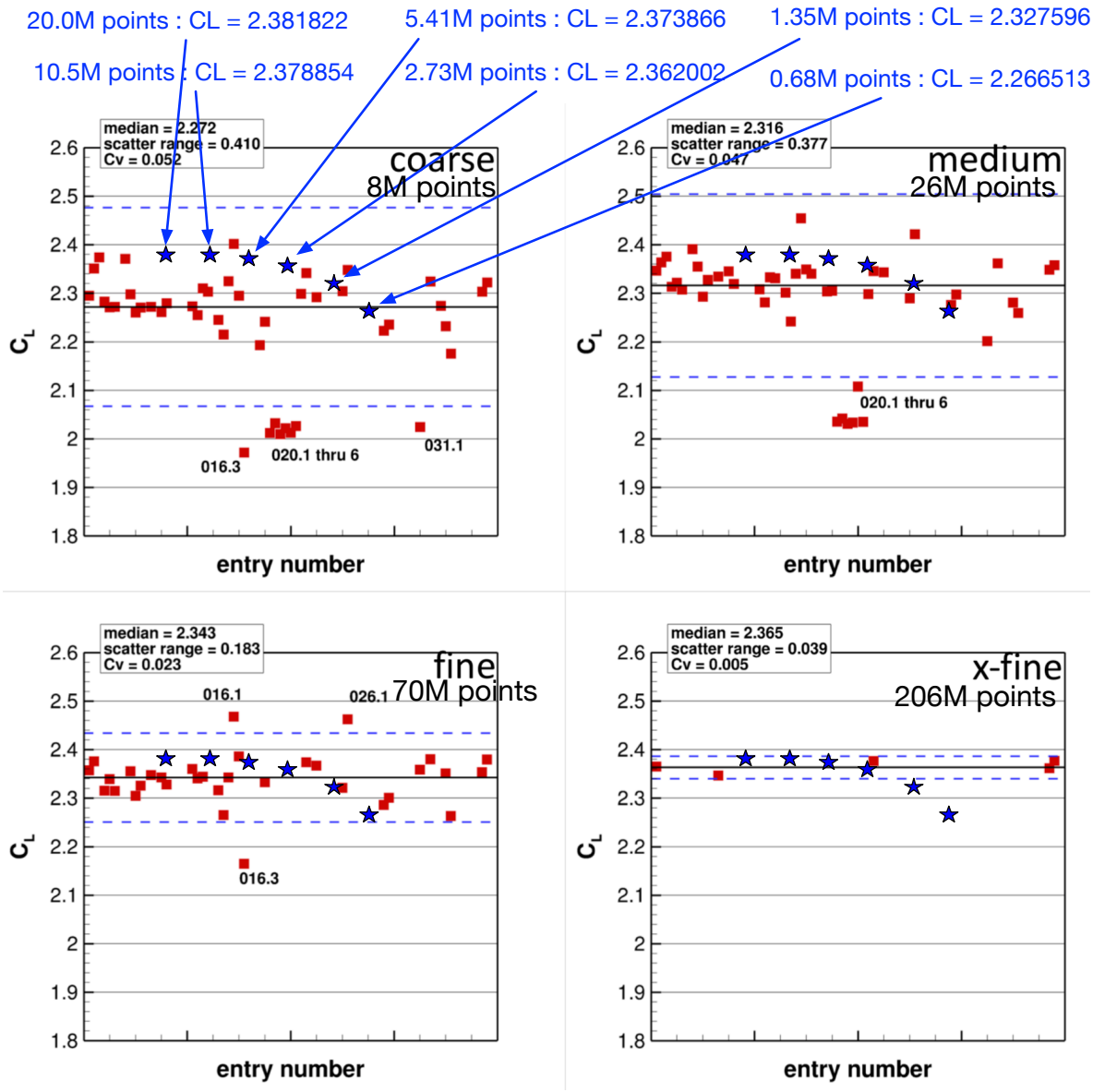

Figure 21. HLPW3 CRM-HL 16° case. Comparison of the lift prediction results obtained with the mesh-adaptive solution platform using the viscous goal-oriented error estimate (blue stars) with respect to all the HLPW3 results (red squares) obtained on the coarse (top left), medium (top right), fine (bottom left) and x-fine (bottom right) meshes.

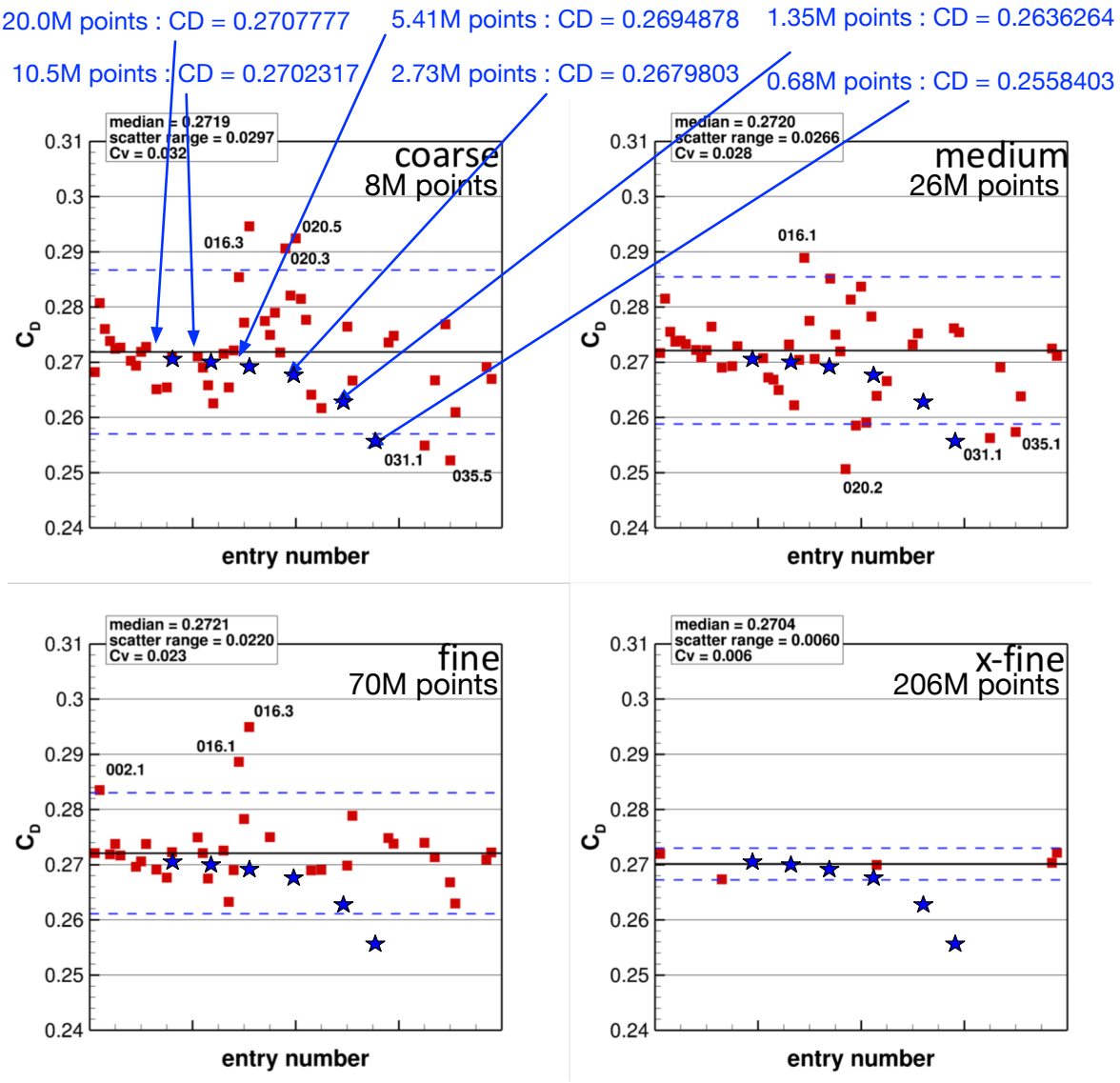

Figure 22. HLPW3 CRM-HL 16° **case. Comparison of the drag prediction results obtained with the mesh-adaptive solution platform using the viscous goal-oriented error estimate (blue stars) with respect to all the HLPW3 results (red squares) obtained on the coarse (top left), medium (top right), fine (bottom left) and x-fine (bottom right) meshes.**

VI. Conclusion

This paper has presented some improvements of the solution-adaptive platform based on the finite volume flow solver WOLF and the adaptive remesher `Feflo.a`. These enhancements have been made in the Newton's method of the flow solver to achieve better convergence on highly anisotropic adapted meshes at each simulation. Mesh-converged and accurate results have been obtained on the 2-D CRM-HL airfoil, and on the CRM-HL geometry of the 3rd AIAA CFD High Lift Prediction Workshop. We have demonstrated on the CRM-HL case that very accurate solutions can be obtained with anisotropic mesh adaptation on pretty coarse meshes made only of tetrahedra. In conclusion, each part of the mesh adaptation platform is a source of improvements

This new strategy has been applied to the High-Lift Common Research Model of the 4th AIAA CFD High Lift Prediction Workshop, see Figure 23. But, it requires larger size adapted meshes to obtain accurate solutions mainly because of the many bracket-induces separation, see Figure 24. Moreover, this more complex case makes the adjoint problem a lot more difficult to solve. This will be addressed in a future publication.

References

[1]F. Alauzet. A parallel matrix-free conservative solution interpolation on unstructured tetrahedral meshes. *Comput. Methods Appl. Mech. Engrg.*, 299:116–142, 2016.

[2]F. Alauzet and L. Frazza. 3D RANS anisotropic mesh adaptation on the high-lift version of NASA's Common Research Model (HL-CRM). In *25th AIAA Fluid Dynamics Conference*, AIAA Paper 2019-2947, Dallas, TX, USA, Jun 2019.

[3]F. Alauzet and L. Frazza. Feature-based and goal-oriented anisotropic mesh adaptation for RANS applications in aeronautic and aerospace. *J. Comp. Phys.*, 439(110340):77 pages, 2021. Available online.

[4]F. Alauzet, L. Frazza, and D. Papadogiannis. Periodic adjoints and anisotropic mesh adaptation in rotating frame for high-fidelity RANS turbomachinery applications. *J. Comp. Phys.*, (110814):65 pages, 2021. Available online.

[5]S.R. Allmaras, J.E. Bussoletti, C.L. Hilmes, F.T. Johnson, R.G. Melvin, E.N. Tinoco, V. Venkatakrishnan, L.B. Wigton, and D.P. Young. Algorithm Issues and Challenges Associated with the Development of Robust CFD Codes. In *Variational Analysis and Aerospace Engineering*, Springer Optimization and Its Applications book series, chapter 1, pages 1–19. Springer, Dordrecht, Heidelberg, London, New York, 2019.

[6]A. Belme, F. Alauzet, and A. Dervieux. An a priori anisotropic goal-oriented estimate for viscous compressible flow and application to mesh adaptation. *J. Comp. Phys.*, 376:1051–1088, 2019.

[7]N.K. Burgess and R.S. Glasby. Advances in numerical methods for CREATE-AV analysis tools. In *52th AIAA Aerospace Sciences Meeting*, AIAA Paper 2014-0417, National Harbor, MD, USA, Jan 2014.

[8]J. Dompierre, M.-G. Vallet, Y. Bourgault, M. Fortin, and W.G. Habashi. Anisotropic mesh adaptation: towards user-independent, mesh-independent and solver-independent CFD. Part III: Unstructured meshes. *Int. J. Numer. Meth. Fluids*, 39:675–702, 2002.

[9]M.C. Galbraith, C.-I. Ursachi, D. Chandel, S.R. Allmaras, D.L. Darmofal, R.S. Glasby, D.L. Stefanski, J.T. Erwin, K.R. Holst, E.A. Hereth, J. Mukhopadhaya, and J.J. Alonso. Comparing multi-element airfoil flow solutions using multiple solvers with output-based adapted meshes. *AIAA Journal*, Published Online, 2021.

[10]W.G. Habashi, J. Dompierre, Y. Bourgault, D. Ait-Ali-Yahia, M. Fortin, and M.-G. Vallet. Anisotropic mesh adaptation: towards user-independent, mesh-independent and solver-independent CFD. Part I: General principles. *Int. J. Numer. Meth. Fluids*, 32(6):725–744, 2000.

[11]R. Haimes and M. Drela. On the construction of aircraft conceptual geometry for high-fidelity analysis and design. *50th AIAA Aerospace Sciences Meeting*, Jan 2012.

[12]A. Loseille and F. Alauzet. Continuous mesh framework. Part I: well-posed continuous interpolation error. *SIAM J. Numer. Anal.*, 49(1):38–60, 2011.

[13]A. Loseille and F. Alauzet. Continuous mesh framework. Part II: validations and applications. *SIAM J. Numer. Anal.*, 49(1):61–86, 2011.

[14]A. Loseille, F. Alauzet, and V. Menier. Unique cavity-based operator and hierarchical domain partitioning for fast parallel generation of anisotropic meshes. *Comput. Aided Des.*, 85:53–67, 2017.

[15]A. Loseille, A. Dervieux, and F. Alauzet. Fully anisotropic goal-oriented mesh adaptation for 3D steady Euler equations. *J. Comp. Phys.*, 229:2866–2897, 2010.

[16]A. Loseille and R. Löhner. Cavity-based operators for mesh adaptation. In *51th AIAA Aerospace Sciences Meeting*, AIAA Paper 2013-0152, Dallas, TX, USA, Jan 2013.

[17]D. Marcum and F. Alauzet. Control of element shape and alignment for 3D solution adaptive mesh generation. *Comput. Aided Des.*, 119:102750, 2020.

[18]T. Michal, D.S. Kamenetskiy, D. Marcum, F. Alauzet, L. Frazza, and A. Loseille. Comparing anisotropic error estimates for ONERA M6 wing RANS simulations. In *56th AIAA Aerospace Sciences Meeting*, AIAA Paper 2018-0920, Kissimmee, FL, USA, Jan 2018.

[19]T. Michal, J. Krakos, D. Kamenetskiy, M. Galbraith, C.-I. Ursachi, M.A. Park, W.K. Anderson, F. Alauzet, and A. Loseille. Comparing unstructured adaptive mesh solutions for the high lift common research airfoil. *AIAA Journal*, 59(9), 2021.

[20]M.J. Pandya, B. Diskin, J.L. Thomas, and N.T. Frink. Improved convergence and robustness of USM3D solutions on mixed element grids. *AIAA Journal*, 54(9):2589–2610, 2016.

[21]C.L. Rumsey, J.P. Slotnick, and A.J. Sclafani. Overview and Summary of the Third AIAA High Lift Prediction Workshop. In *56th AIAA Aerospace and Sciences Meeting*, AIAA-2018-1258, Kissimmee, FL, USA, Jan 2018.

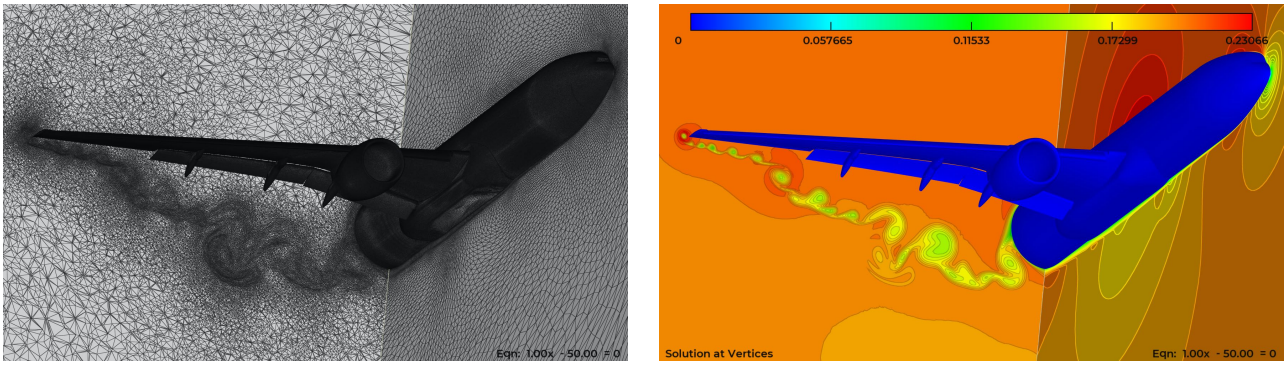

Figure 23. HLPW4 CRM-HL 7° case. Adapted mesh composed of 20M vertices and associated solution field (local Mach number) for the cut plane $x = 50$.

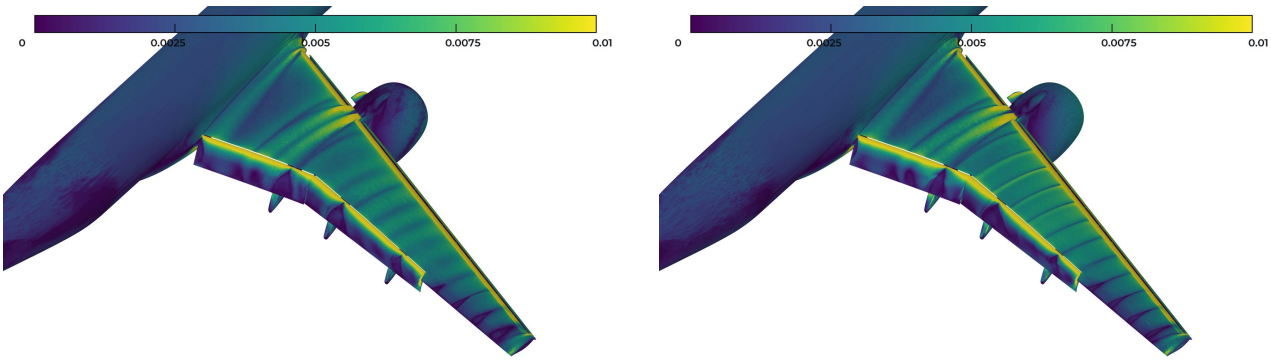

5M of vertices 35M of vertices

Figure 24. HLPW4 CRM-HL 7° case. Surface Cf contours obtained for an adapted mesh composed of 5M vertices (left) and $35M$ vertices (right).